scientific reports

Check for updates

OPEN

Microstructure evolution and catalytic activity of AlCo$_{1-x}$FeNiTiMo$_x$ high entropy alloys fabricated by powder metallurgy route

Maria Sveda[1], Ferenc Kristály[2], Emőke Sikora[3], Anna Sycheva[1], Gábor Karacs[1], Tibor Ferenczi[4] & Dora Janovszky[1]✉

This investigation presents the synthesis of equiatomic and non-equiatomic AlCo$_{1-x}$FeNiTiMo$_x$ (x = 0, 0.1, 0.25 and 1.0) high entropy alloys fabricated by mechanical alloying. Mo partially replaced Co. Classic thermodynamic calculations, such as mixing enthalpy (ΔH_{mix}), configurational entropy (ΔS_{mix}), the atomic size difference (δ), entropy to enthalpy ratio (Ω), electronegativity difference ($\triangle\chi$), and valence electron concentration (VEC) were used. Considering δ, Ω and VEC parameters, a BCC solid solution and an intermetallic phase can be predicted due to the partial replacement of Co by Mo. X-ray and electron diffraction of equiatomic HEA without Mo content revealed that after 35 h of milling, a Fe-type BCC lattice phase was formed in the alloy and two L2$_1$ phases, in addition to a minimal amount of FCC phase. As the Mo content increased, the Fe-type BCC phase was steadily replaced by the Mo-type BCC phase and the Fe-type FCC phase, and two L2$_1$ phases were also developed. When the 5 at% Mo-containing (x = 0.25) alloy was further milled for 80 h, the amount of phases remained almost the same; only the grain size was strongly reduced. The influence of the Mo addition on the properties of studied alloys was also confirmed in the decolourisation of Rhodamine B using a modified photo-Fenton process. The decolourisation efficiency within 20 min was 72% for AlCoFeNiTi and 87% for AlCo$_{0.75}$FeNiTiMo$_{0.25}$ using UV light with 365 nm wavelength.

Keywords High entropy alloys, Dye decolourisation, Ball milling method

In 2004, Yeh[1] and Cantor et al.[2] published the possibility of producing multi-component high-entropy alloys (HEAs). Conventional alloys have one main constituent (e.g., Fe, Al, Cu) whose properties significantly affect the alloy. In contrast, with HEAs, there is no main constituent, but all the components together influence the properties of the alloy. HEAs have extraordinary properties such as high hardness[3], high strength at room temperature[4] even at elevated temperatures[5], and excellent resistance to wear[6] and corrosion[7,8]. The microstructure of HEA can vary greatly depending not only on the nature and quantity of the constituent elements but also on the manufacturing conditions. The first HEAs were pure solid solutions with face-centred cubic (FCC) or/and body-centred cubic (BCC) lattices[9–11]. As more and more HEAs were produced, the second-generation HEAs already include many types: TRIP-TWIP HEAs[12], precipitation-strengthening HEAs[13], eutectic HEAs[14], interstitial strengthening HEAs[15], and amorphous[16,17] ones. The selection of the constituent elements is a crucial step. There are currently many empirical rules for material design[18], and their number is growing. As the number of HEAs produced increases, more and more experiences are accumulated. Since 2020, much research has focused on the favourable catalytic properties of HEA alloys[18–22]. Fe, Ni, and Co are known to act as catalysts in water splitting[23]. Open circuit potential (OCP) values of pure elemental metals (Mo, Cr, Co, Al, Mg) measured under the same conditions showed that the highest value of OPC was Mo, indicating that adding Mo can increase electron transfer[20]. Mo has an excellent effect on the electrocatalyst for oxygen evolution reaction[24–26].

[1]HUN-REN-ME Materials Science Research Group, University of Miskolc, Miskolc, Hungary. [2]Department of Geology and Mineral Deposits, University of Miskolc, Miskolc, Hungary. [3]Institute of Chemistry, University of Miskolc, Miskolc, Hungary. [4]Institute of Foundry and Metallurgy, University of Miskolc, Miskolc, Hungary. ✉email: fekjd@uni-miskolc.hu; drczelgyorgyne@gmail.com

1

Sample	Equipment	Ball to powder ratio	PCA	Milling time and speed	Structure of powder	Structure of bulk sample	Refs.
AlCoFeNiTi	Planetary ball mill	10:1	45 h dry milling + 4 h ethanol	45 h at 300 rpm	main BCC+ a few FCC	Spark plasma sintering a primary FCC + a BCC + a trace amount of Al_3Ti	27
AlCoFeNiTi	Fritsch P-5	10:1	Toluene	300 rpm	BCC	SPS: BCC + TiC	28
AlCoFeNiTi	Fritsch P-5	10:1	Toluene	8 h 300 rpm	BCC	SPS: two BCC (2.95 Å) + BCC(B2 2.916 Å) + TiC	29
AlCoFeNiTi	SPEX 8000 M	10:1	Methanol	15 h	BCC	conventional sintering: BCC (2.87 Å) + FCC1(3.60 Å) + FCC2(4.27 Å)	30
AlCoFeNiTi		25:1	Toluene	30 h 400 rpm	main FCC (3.571 Å) + a few BCC (2.858 Å) + Ni_4Ti_3	-	31
AlCoFeNiTi	Arc furnace + water-cooled copper mould				-	ingot: $L2_1$(Fe_2AlTi) + BCC1(Fe, Co, Ni)+ BCC2(Fe, Al Ti) plate: $L2_1$ + BCC2	32
AlCoFeNiTiMo	SPEX 8000 M	10:1	methanol	15 h	BCC1 Mo-type + BCC2 Fe-type + FCC	FCC1(3.60 Å) + FCC2 + Co_7Mo_6	30
AlCoFeNiTiMo	SPEX 8000 M	5:1	methanol	20 h	BCC1 Mo-type BCC2 Fe-type	conventional sintering: FCC + BCC Fe-type, +μCoMo-type + α CoMo-type arc melted ingot: BCC Mo-type, Ti_2O	33

Table 1. Conditions of experimental and microstructure characteristics of equiatomic AlCoFeNiTi, AlCoFeNiTiMo HEA alloy samples reported in the literature.

Properties	Fe	Ni	Co	Mo	Al	Ti
r (Å)	1.241	1.246	1.251	1.363	1.432	1.462
T_m (K)	1811	1728	1768	2896	933	1941
VEC	8	10	9	6	3	4
χ	1.83	1.54	1.88	2.16	1.61	1.91
Structure	BCC	FCC	HCP + FCC	BCC	FCC	HCP
HV(MPa)	608	638	1043	1530	167	970

Table 2. Properties of pure elements constituting the $AlCo_{1-x}FeNiTiMo_x$ (x = 0, 0.1, 0.25, 1.0) HEAs (the metallic atomic radius (r), the melting temperature (T_m), average valence electron concentration (VEC) and the Pauling electronegativity (χ) and structure. The atomic radius, average valence electron concentration, and Pauling electronegativity are taken from Ref[34].

In the current work, an alloy was selected as the base alloy, which several authors tested in the literature. No consistent results were found regarding the phases formed (Table 1). Based on the literature study, the resulting structure of these compounds is highly dependent on the production method.

Mechanical alloying was designed and produced in the present study AlCo1-xFeNiTiMox (x = 0, 0.1, 0.25 and 1) HEA powders. In addition to the base alloy, we developed a new, non-equiatomic and equiatomic composition. We investigated the effect of the mechanical milling and Mo content on structural transformation, the thermal stability and the dye decolorisation. In the literature, Mo has been added to the basic composition as a new combining element in the same atomic proportion as the other elements. Co is an important element in catalyst alloys and the partial or total substitution of Co by Mo has not been investigated. Hydrogen as an energy carrier is increasingly being explored. In ammonia decomposition, HEAs containing Mo have produced very favourable results[22]. It is, therefore, important to investigate whether its role in water purification could be beneficial. The relevant literature does not discuss the effect of Mo in water purification, especially when Mo as a catalyst atom completely replaces Co in the HEA alloy. All these shortcomings are purposefully addressed in the present publication.

Materials and methods
Preparation of HEA powders and samples
High-purity powders of Al (99.5 pure, < 45 μm size), Co (99.8% pure, 150–45 μm size), Fe (99% pure, < 75 μm size), Ni (99.8% purity, 100–75 μm size), Ti (99.4% pure, < 150 μm size), Mo (99.95% pure, 3–7 μm size) have been used in this work. The properties of the initial elements are summarised in Table 2. These powders were ball milled in an argon atmosphere in a planetary ball mill (Fritsch, Pulverisette 5). Balls were selected from hardened steel. A combination of balls with different diameters was used for milling: 5 balls with 20 mm diameter, 14 balls with 12 mm diameter, 4 balls with 10 mm diameter and 10 balls with 7 mm. Given that Fe is already present in the composition, the effects of possible Fe transportation from balls to powders on the mechanical properties are marginal. The ball-to-powder ratio was 13:1, and the milling speed was 200 rpm. In the case of Mo0 and Mo0.25, the milling process was interrupted every 5 h. The maximum milling time for all alloys was 35 h, except for Mo0.25, where milling was continued for 80 h. Each 1 h milling process was followed by 1 h to cool down the vials. Toluene was used as a process control agent (10 ml). For convenience, the produced AlCoFeNiTi,

AlCo$_{0.875}$FeNiTiMo$_{0.1}$, AlCo$_{0.75}$FeNiTiMo$_{0.25}$ and AlFeNiTiMo HEA powders were referred to as Mo0, Mo0.1, Mo0.25 and Mo1.0 respectively.

Methods

The composition of samples was examined with a Bruker D8 Advance diffractometer (XRD) using Cu Kα radiation (40 kV, 40 mA), in parallel beam geometry obtained with a Göbel mirror equipped with a Vantec-1 position sensitive detector (1° window opening), measured in the 2-100 °(2 θ) angular range, at a 0.007° (2 θ)/29-sec speed. The specimen was rotated in the sample plane during the measurement to obtain data from the whole surface and to reduce in-plane preferred orientation effects. The microstructure of the powders was analysed by a Scanning Electron Microscope (Thermo Scientific Helios G4 PFIB SEM) equipped with an Energy Dispersive Spectrometer (EDS) and Hitachi S-4800 FE-SEM. Transmission electron microscopy (TEM, Tecnai G2) was used for microstructural characterisation through selected area electron diffraction (SAED). TEM/SAED patterns were processed and converted to diffraction profiles using the Crisp 2.1 program. The specific surface area of the HEA powder was examined using the Brunauer–Emmett–Teller method (BET, Micrometrics TriStar 3000). Nitrogen adsorption-desorption isotherms were acquired at 77 K using. The particle size distributions were done on the SEM images based on measuring 500 grains.

Decolourisation of RhB (C$_{28}$H$_{31}$ClN$_2$O$_3$, Fluka AG) under UV light irradiation experiments of the HEA samples was evaluated. In every experiment, eight parallel reaction mixtures were prepared as follows: 50 mg sample was added for 25 mL of RhB solution (5 mg/l). After mixing the powder samples and RhB solutions, the samples were simply stirred on a magnetic stirrer for 15 min. The sample analysed after 15 min has been named the sample for time '0'. We wanted to see if adsorption would occur and if the dye would be bound by the HEA, but we measured negligibly small concentration differences so that we did not have to expect adsorption during the process. After that, 0.25 mL of hydrogen peroxide solution (H$_2$O$_2$, 50 wt %) was injected into the solutions, and the irradiation started. The initial pH of the rhodamine solution was 7.2 pH of the reaction mixture was not controlled during the catalytic reaction. At certain time intervals, 1–1 sample was taken from the magnetic stirrer and has been filtered. The RhB concentration of the filtrates was determined using an EMITA VP-60 UV lamp (power 180 W). It transmits UV radiation in the range of 320–400 nm; the maximum emission was at 365 nm wavelength.

Results and discussion

Prediction of phase formation for the designed HEA

Today, no rules can be used to predict the development phases for a given composition of HEAs. This is understandable because there are many aspects to consider when a phase forms: thermodynamic and kinetic factors. Intensive research is now underway to predict the phases in a multi-component system. Phase diagrams for alloys with 5–6 constituents are only available in limited numbers, so the empirical criteria for HEAs are used to predict phases in high entropy alloys. Zhang et al.[35] three parameters have been introduced which can be used together to characterise the impact of the constituent elements of the HEA: the mixing enthalpy (ΔH_{mix}), the mixing entropy (ΔS_{mix}) and the atomic size difference (δ). Guo et al.[34] reviewing the HEAs in the literature, they conclude that a solid solution is formed, and only if all three parameters are satisfied that - $-22 \leq \Delta H_{mix} \leq 7$, $11 \leq \Delta S_{mix} \leq 19$ and atomic size difference (δ) < 8.5. Partial and total replacement of Co by Mo resulted in a slight decrease in the atomic size difference (Table 3). The results of the calculated parameters are shown in Table 3. The calculated values for the designed alloys of this study, the combination of the three parameters, are met only by the AlFeNiTiMo composition, with a high probability of solid solution (SS) formation for this alloy and intermetallic phase (IM) formation expected for the other alloys.

Yang et al.[36] proposed a parameter (Ω), which is a parameter used to assess the phase stability of the HEA. According to Yang's criterion, none of the alloys studied in this work complete this; a stable solid solution cannot be expected.

Gao et al.[37] introduced two new parameters: the electronegativity difference, $\Delta \chi$, and the valence electron concentration (VEC). The VEC values decrease with Mo content (Table 3). The calculated VEC values are all less than 6.87, so a BCC phase is expected for each alloy.

Samples	ΔH_{mix}*, kJ/mol	ΔS_{mix}, J/(molK)	δ, %	Ω-	T_m, K	VEC	$\Delta \chi$	ΔG_{mix}, kJ/mol	Expected phase formation	Structure
AlCoFeNiTi	-26.40	13.38	7.46	0.83	1636	6.80	0.15	-39.5	IM	BCC
AlCo$_{0.9}$FeNiTiMo$_{0.1}$	-26.00	13.92	7.43	0.89	1659	6.74	0.16	-40.0	IM	BCC
AlCo$_{0.75}$FeNiTiMo$_{0.25}$	-25.35	14.32	7.33	0.96	1693	6.65	0.17	-39.9	IM	BCC
AlCo$_{0.5}$FeNiTiMo$_{0.5}$	-24.20	14.53	7.18	0.98	1749	6.50	0.19	-39.5	IM	BCC
AlCo$_{0.25}$FeNiTiMo$_{0.75}$	-23.11	14.32	7.01	1.01	1805	6.35	0.21	-38.6	IM	BCC
AlCo$_{0.0}$FeNiTiMo$_{1.0}$	-21.60	13.38	6.80	1.00	1862	6.20	0.22	-36.5	SS	BCC

Table 3. The calculated values of parameters (ΔH_{mix}, ΔS_{mix}, δ, Ω, T_m, VEC and $\Delta \chi$) for the investigated alloys. *IM* intermetallic, *SS* solid solution. *The binary mixing enthalpies in ternary amorphous systems used in the calculation can be found in Ref[38].

Microstructure of milled powder

Representative microstructure micrographs of the initial and milled powders are in Fig. 1. The initial size of the metallic particles varied from 1 μm to 150 μm, and the particles were nearly roundish-shaped. The darkest gray-coloured particles correspond to Al powder in backscattered SEM atomic number-sensitive images. In contrast, Ni particles are the lightest (Fig. 1a). Drastic changes occurred in the powder mixture after 5 h milling. It can be seen that the initial particles have lost their shape, with the larger particles being sheared by the balls into flat, thin, disc-shaped particles and the smaller ones being crushed. Ni and Co were only detectable on the surface of the powder particles after 5 h of milling (Fig. 1b). Much of the surface of the powders is now the same colour, showing that the solid solution has started to form (Fig. 1b). After 10 h milling time, besides the 2–3 μm
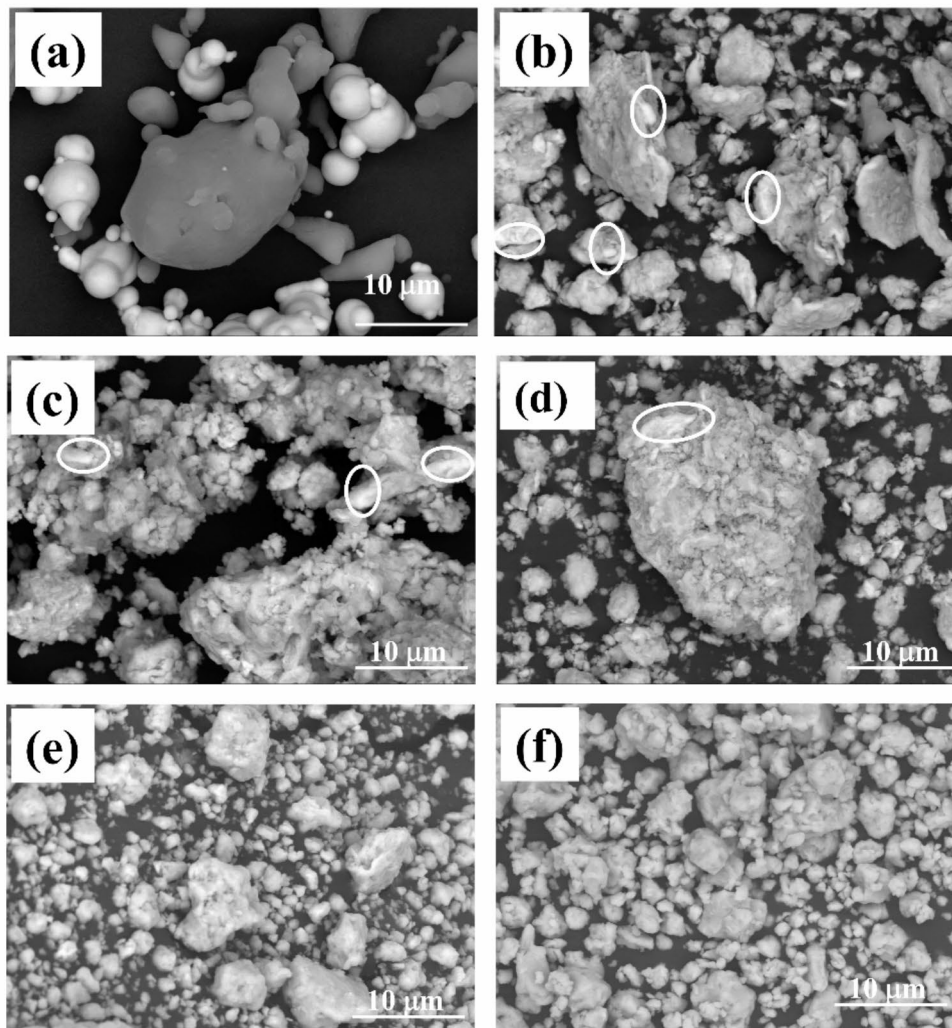
Fig. 1. Evolution of morphology of AlCoFeNiTi composition powder leading to HEA powder production: powder mixture before milling (**a**); after 5 h (**b**), 10 h (**c**), 15 h (**d**), 20 h (**e**), 30 h of ball milling (**f**). The areas marked with a white circle show Ni and Co elemental powder particles.

particles, large agglomerates of these smaller particles are formed. After 10 and 15 h of milling, some pure elemental metal particles were detectable on the surface (Fig. 1c,d). Due to continuous fractures, the average grain size constantly decreases, but agglomeration is also significant (Fig. 1c,d). Agglomerates are much smaller after 20 and 30 h (Fig. 1e,f). After 35 h of milling, most particles are below 10 microns in size (Fig. 2a,b). The presence of Co, Al and Ti enrichment in the cross-section of the grains was visible only in grains larger than 20
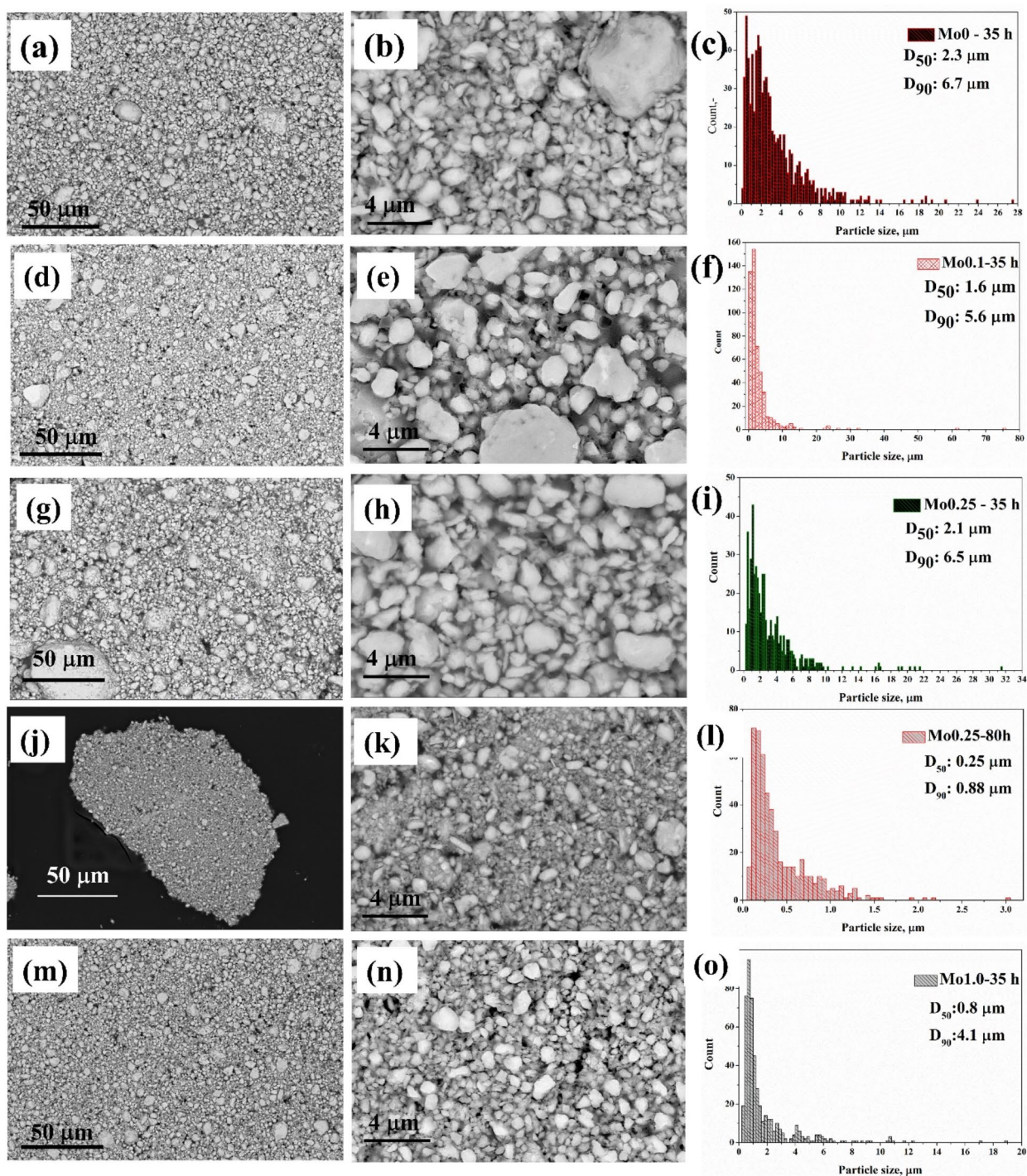
Fig. 2. Cross-section SEM images and particle size distributions of Mo 0,0 powders milled for 35 h (**a–c**), Mo0.10 (**d–f**), Mo0.25 (**g–i**) powders and Mo0.25 milled for 80 h (**j–l**), Mo 1.0 (**m–o**).

micrometres but not near the surface. However, such grains were not seen in significant amounts (Fig. 2c). The median value of the particle size distribution is 2.3 μm (Fig. 2c).

When cobalt was partially replaced by 2 at% (Mo0.1) molybdenum, the microstructure of the powders was investigated after 35 h. The grains are less spherical when examining the cross-section of the powders after 35 h of milling (Fig. 2d,e). The median particle size distribution value is 1.6 μm (Fig. 2f). In the case of 5 at% molybdenum (Mo0.25), the microstructure of the powders was investigated after 35 h and 80 h. The grain edges are rounded after 35 h of milling (Fig. 2g,h). The median particle size distribution value is 2.1 μm (Fig. 2i). The fragmentation is very pronounced after 80 h of grinding (Fig. 2j,k). There are aggregates between 20 and 100 microns, made up of particles smaller than 4 microns, but many of them are less than 1 micron (Fig. 2k). Notably, some grains are elongated and noodle-shaped (Fig. 2k). The median particle size distribution value is 0.25 μm (Fig. 2l). In the case when Mo is fully substituted for Co, then very small particle sizes can be seen along with larger than 2 μm particles (Fig. **2**m,n). The median value of particle size distribution is 0.8 μm (Fig. 2o). Looking at the particle size distribution, it can be seen that the smallest particle size is Mo0.25–80 h, followed by Mo1.0–35 h and Mo0.1–35 h. Mo0. 25–80 h, but these small grains aggregated to form agglomerates, while for Mo0.1–35 h and Mo1.0–35 h, no agglomerates were formed from the large and small grains, and 90% of the grains were smaller than 5.6 μm and 4.1 μm, respectively.

Figure 3a shows the XRD plot for AlCoFeNiTi alloy with varying milling times. The initial elementary powder's reflections are clearly visible in the unmilled sample. During the high-energy milling, the powder particles repeatedly collide, fragmenting and cold-welding. As the particle size decreases, the diffusion path decreases. The free volume in the crystals changes continuously during grinding, increasing the diffusion of atoms, which accelerates the formation of solid solutions. According to the melting point theory named by Alam et al.[39], the disappearance or persistence of peaks in an XRD pattern for mechanically alloyed material depends on the melting point of the constituting elements. Elements with a lower melting point disappear after a shorter milling time than those with a higher melting point, i.e. they are incorporated into a solid solution sooner. Chen et al.[40] also found this alloying sequence in the $Cu_{0.5}NiAlCoCrFeTiMo$ alloy system. In the AlCoFeNiTi alloy system, according to this theory, the alloying sequence is Al→Ni→Co→Fe→Ti. Based on the X-ray and SEM-EDS elemental mapping, Al is dissolved after 15 h of milling. One of the most common constituents of HEA alloys is Al. Although Al is an FCC lattice metal, its presence in HEA alloys favours the formation of the BCC lattice[41]. According to the theory of Alam et al.[39], after Al and Ni, Co should have homogeneously dissolved in the powder mixture during the formation of the HEA alloy. However, Co enrichment can still be detected in the cross-section of very few particles larger than 25 μm, even after 35 h of milling. We looked for a possible explanation. Co is the hardest of the five elements but a ductile metal. In the initial powder, Co has a hexagonal cubic structure(HCP) + FCC mixture structure. Sort et al.[42] demonstrated that the FCC ⟷ HCP phase transformation occurs several times during high-energy milling; the direction of the transformation depends on the milling time, and after a long milling time, a near-equilibrium state is reached between the two structures. We also observed a change in the Co HCP/FCC structure ratio during milling. Allotrope transformation of the Co element influences the formation of new metallic phases during milling. The reflections of elementary powders during milling gradually disappear, except for peaks characteristic of a BCC lattice type, as the HEA solid solution structure is formed. The milling processes were different when cobalt was partially or entirely replaced by molybdenum (Fig. **3**b). Mo powder has the smallest initial particle size in this alloy system; Mo is ductile and the hardest of the milled powders. After 35 h of milling, the most remarkable feature of the XRD images was that the Mo peak had been retained.

The qualitative and quantitative identification of the phases formed in the milled powders was carried out using the Rietveld method. The refined diffraction pattern of powder milled for 35 h obtained is given in Fig. 4.
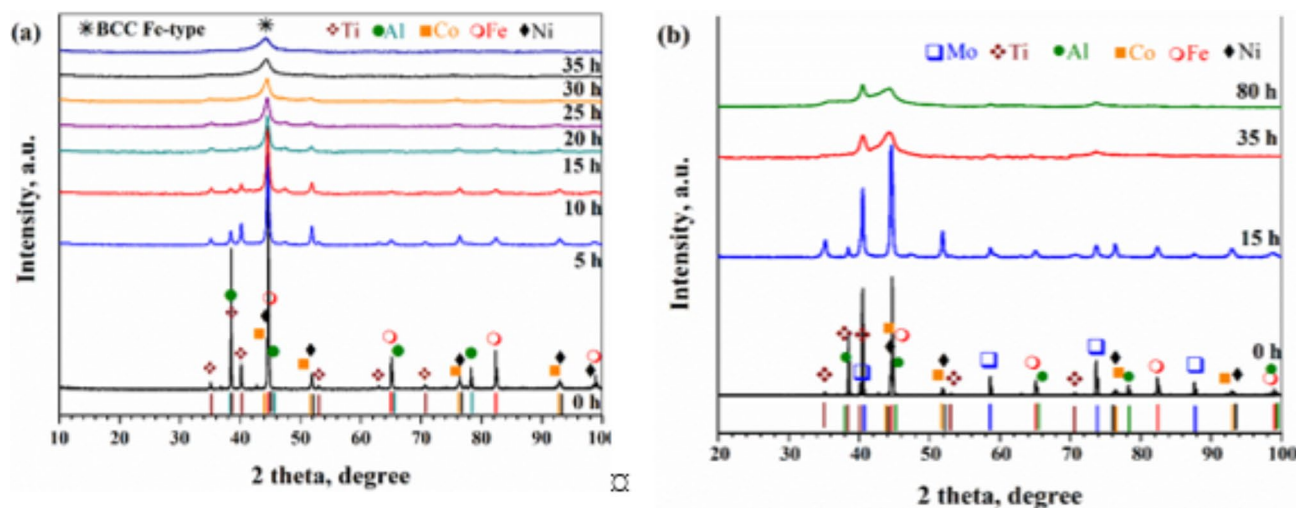

Fig. 3. Microstructure change depending on the milling time of AlCo$_{1-x}$FeNiTi Mo$_x$ powders alloy (X = 0;0.25).
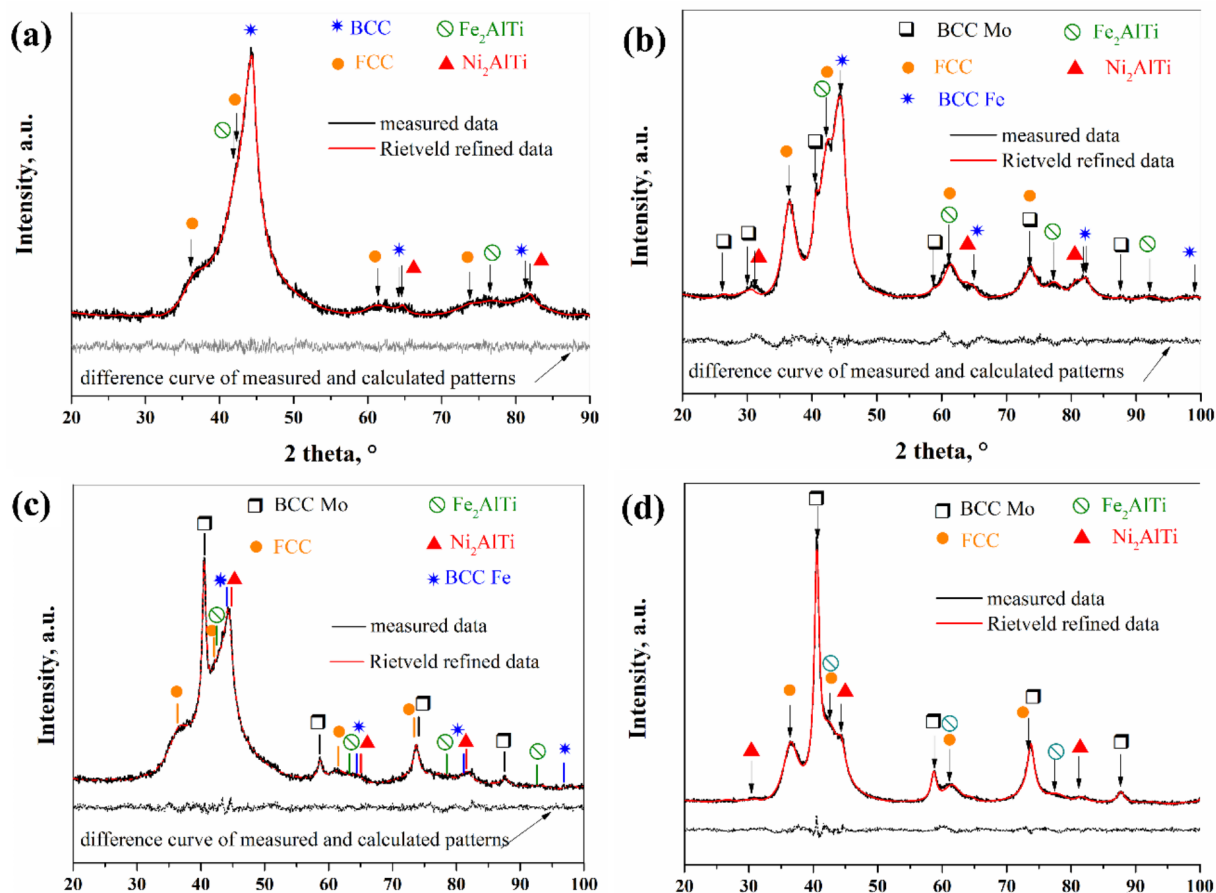
Fig. 4. Rietveld refinement diffraction patterns of $AlCo_{1-x}FeNiTiMo_x$ powder milled for 35 h: AlCoFeNiTi (**a**), $AlCo_{0.9}FeNiTiMo_{0.1}$ (**b**), $AlCo_{0.75}FeNiTiMo_{0.25}$ (**c**), AlFeNiTiMo (**d**) (Ni_2AlTi phase is PDF #65–0432 card, FCC is the HEA phase developed from austenite prototype structure).
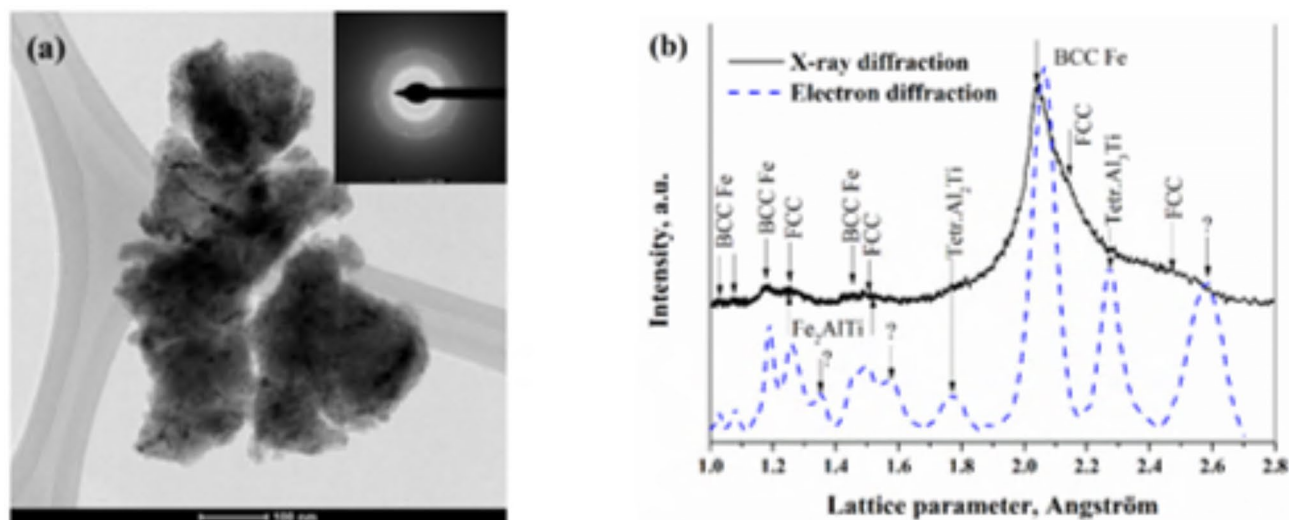

Fig. 5. TEM and the corresponding SAED pattern (in the inset) images (**a**) of as-milled Mo0 powder after 35 h of milling in a bright field; comparison of TEM/SAED patterns with XRD diffraction pattern (**b**).

Sample	Lattice parameter, nm				
	BCC Fe	BCC Mo	FCC	Fe$_2$AlTi	Ni$_2$AlTi
Mo0	0.29029	--	0.42560	0.60876	0.57540
Mo0.1	0.28716	0.31459	0.42689	0.60500	0.58321
Mo0.25–35 h	0.28938	0.31476	0.42735	0.61641	0.59576
Mo0.25–80 h	0.28926	0.31472	0.42672	0.59952	0.57700
Mo1	–	0.31474	0.42684	0.59900	0.57800

Table 4. Variation of lattice parameter in HEA powders with compositions and milling time.

Sample	BCC Fe		BCC Mo		FCC		Fe$_2$AlTi		Ni$_2$AlTi	
	wt%	Crystallite size, nm	wt%	Crystallite size, nm	wt%	Crystallite size, nm	wt%	Crystallite size, nm	wt%	Crystallite size, nm
Mo0	43	3 ± 1	-	-	14	2 ± 1	28	3 ± 1	15	9 ± 3
Mo0.1	16	7 ± 1	3	10 ± 3	25	4 ± 1	37	3 ± 1	19	6 ± 2
Mo0.25–35 h	27	4 ± 1	14	13 ± 3	14	2 ± 1	35	2 ± 1	10	6 ± 1
Mo0.25–80 h	22	5 ± 1	15	14 ± 3	13	3 ± 1	38	3 ± 1	12	7 ± 1
Mo1	–	–	30	10 ± 3	31	3 ± 1	24	3 ± 1	15	6 ± 1

Table 5. Weight fraction and crystallite size in HEAs powder.

In the case of Mo0 power, the reflections showed a BCC structure (43 wt%) with a lattice parameter of 0.2888 nm (Fig. 4a; Table 4), indicating that it corresponds to the Fe-type BCC(Im-3m) structure. This lattice parameter was larger than the pure Fe element (a$_{Fe}$= 0.2866 nm). This phase contains all chemical elements (Al, Co, Ni, and Ti). Fe has the smallest atomic diameter in this alloy system, so incorporating atoms from all the other elements in the solid solution increases the lattice parameter. In addition to the BCC lattice Fe-type phase, an FCC (Fm-3m) lattice phase (14 wt%) and two L2$_1$ (Heusler type, Ni$_2$AlTi and Fe$_2$AlTi)) phases were identified (Fig. 4a; Table 5). The Ni-based L2$_1$ was identified from the ICDD PDF database, and Rietveld refinement returned a good fit for its theoretical lattice parameters and atomic coordinates. On the fitting residual, the peaks corresponding to a Fe-based L21 were revealed, which in turn was not found in the PDF database, but replacing Ni with Fe in the prototype structure and refining lattice parameters. The calculated density values The calculated density values are Ni$_2$AlTi 6.703 g/cm^3, Fe$_2$AlTi 5.493 g/cm^3, BCC 7.582 g/cm^3 and FCC 7.753 g/cm^3. These L2$_1$ phases play a significant role in the excellent mechanics of 3d high-entropy alloys[43]. The lattice parameters and crystal sizes are given in Tables 4 and 5. Beyond the L2$_1$ phases, the diffracted intensities (broad and overlapping peaks) could be resolved by using the alpha-Fe BCC and austenite FCC structures as prototypes and refining the lattice parameters while approximate atomic alloying ratios were set based on the initial metal ratios. The crystallite size was below 10 nm owing to high energy milling. Comparing the X-ray results with literature data, Fu et al.[27] also identified BCC and FCC phases in the powder but did not find L2$_1$ phases.

The milling processes were different when cobalt was partially replaced by 2 at% molybdenum (Mo0.1). After 35 h of milling, the most remarkable feature of the XRD image is the appearance of four phases in addition to the BCC Fe-type phase (Fig. 4b). The amount of BCC Fe-type phase was reduced to 16 wt%. The lattice parameter of the Fe-type phase is 0.28716 nm, which is higher than the lattice parameter of pure Fe but lower than the lattice parameter of BCC without Mo content (Table 4). BCC Mo-type with 3 wt% phase formed during high-energy milling. The lattice parameter of this phase was smaller than pure Mo (a$_{Mo}$ = 0.31472 nm Table 4). Mo can dissolve very few elements, according to the biner phase diagrams. Of the possible elements, only the Mo-Ti solid solution is formed according to the equilibrium phase diagrams. Fe, Ni and Co have smaller atomic diameters than Mo. Al and Ti have greater atomic diameters than Mo. Fe, Co and Ni were incorporated into the Mo lattice in higher proportions due to high-energy milling. Two L2$_1$ (Heusler) phases compound coexisted in powder milled of 35 h (Fig. 4b). This milled alloyed powder contained the highest intermetallic phases (37 wt% Fe$_2$AlTi phase and 20 wt% Ni$_2$AlTi). An FCC phase is also formed with a lattice parameter of 0.42688 nm.

In the case of 5 at% Mo (Mo0.25), after 35 h of milling, the lattice parameters of each phase increased in comparison with Mo0.1 (Table 4). The same phases were identified in this sample as in Mo0.1 (Fig. 4c), but the amount of phases changed (Table 5). The amount of the BCC Fe phase almost doubled, while the amount of the FCC phase was nearly halved. The weight fraction of BCC Mo phase volume increased fourfold, resulting in solid solutions of 55 wt%. A literature review shows that an equiatomic AlCoFeNiTiMo alloy was prepared by high-energy milling. Rubio et al.[30] identified a type of BCC lattice phase in the powder after 15 h of milling and an FCC phase. Lopez et al.[33] identified two types of BCC structure phases (a Fe-type and a Mo-type) in the powder after the 20-hour milling process. In our case, the non-equiatomic composition was only 5 at% Mo content, but this small amount was not entirely incorporated into the Fe-type BCC lattice; another Mo-based BCC phase has developed. One BCC phase was successfully formed in the literature for 10 at% Mo added to AlCoCrNi high entropy alloy[44]. The milling was further carried out to see if converting the Mo-type and Fe-type BCC phases into a single solid solution is possible. However, after 80 h, the amount of phases varied up to 5 wt% in favour of intermetallic phases. This shows that the L2$_1$ phases are very stable; they did not disappear due

to the additional energy input, and only the BCC and FCC phases would have formed. The lattice parameters decreased for all phases compared to 35 h milling.

In the case of Mo1 (20 at%), after 35 h milling time, the XRD image confirmed a BCC Mo-type, an FCC phase and two L2$_1$ phases (Fig. 4d). The combined amount of BCC and FCC solid solutions is 61 wt%. BCC Mo-type phase was the phase with the largest crystallite size during the milling process with Mo content (10–13 nm).

The powders were also analysed using a TEM image to justify the crystal size of the phases obtained in the nanoscale. The HEA particles on thin carbon film (Fig. 5a) represent some agglomerations and exhibited diffractions in the TEM/SAED pattern of the mechanically alloyed Mo0 powder for 35 h. TEM/SAED patterns were processed and converted to a diffraction profile (see Fig. 5b). Compared to the X-ray and electron diffractograms, it can be seen that the curves are in good agreement. The wavelength of 200 keV accelerating voltage is 0.0274 Å, and the X-ray diffraction measurement is 1.5418 Å. Therefore, electron diffraction has a higher resolution. It is, thus, understandable that new peaks appeared in the electron diffraction measurements. One tetragonal structure phase containing aluminium and titanium was identified by electron diffraction: This Al$_3$Ti intermetallic phase has a variable composition[45]. An FCC lattice peak was also identified. Some peaks have not been identified.

TEM studies of Mo0.25 were also carried out to obtain more information about the phases. TEM/SAED rings (Fig. 6a) converted to a diffraction profile (Fig. 6b). The electron diffraction measurement shows a BCC Fe-type, BCC Mo-type and an FCC phase at the amorphous-crystalline interface, confirming the X-ray crystal size results (Table 5). Based on the elemental mapping of STEM EDX elemental map, tanks to high-energy milling, elements with atomic diameters smaller and larger than Mo can be incorporated into the Mo lattice (Fig. 6c).
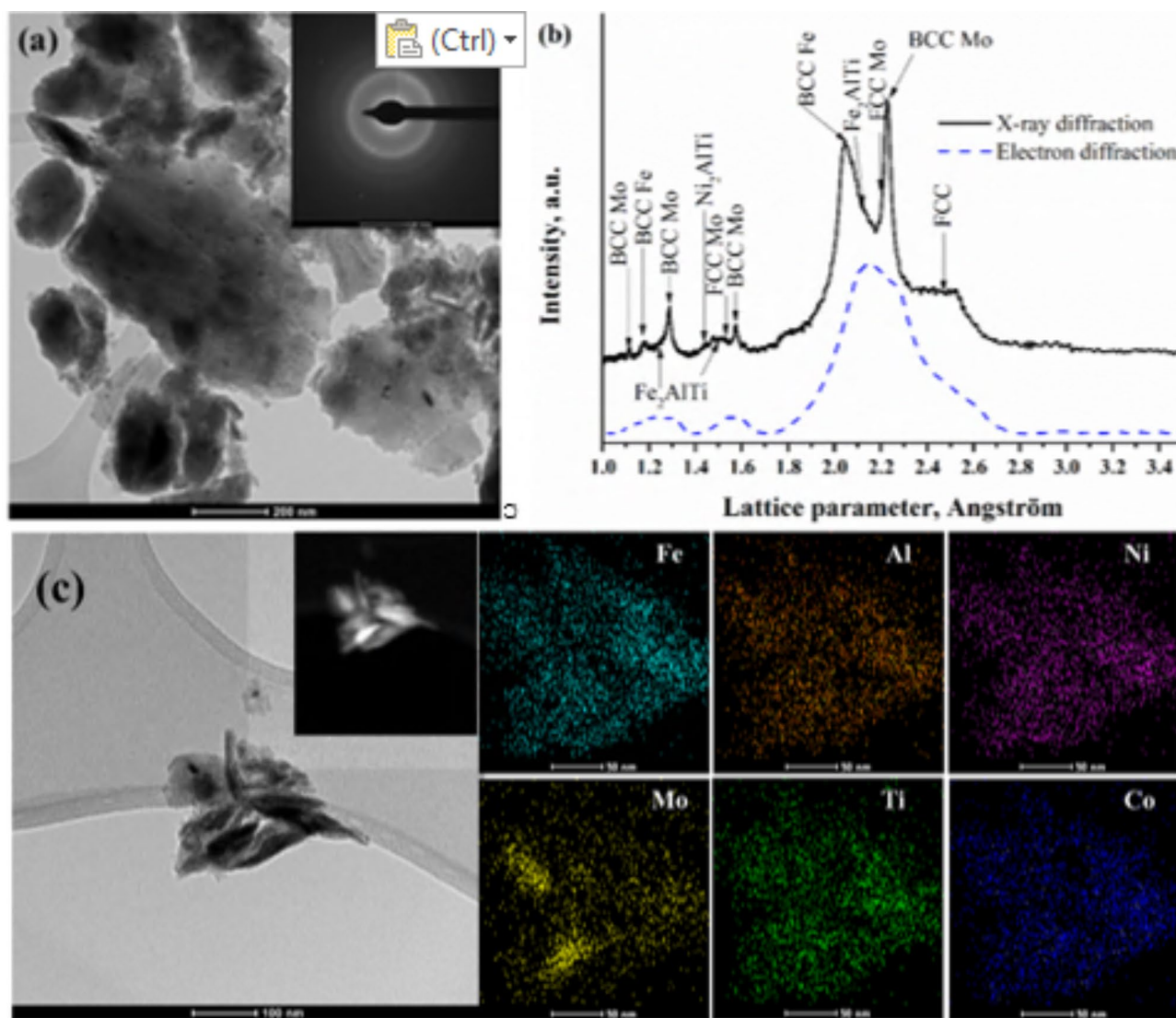

Fig. 6. TEM micrographs of as-milled AlCo$_{0.75}$FeNiTiMo$_{0.25}$ powders after 80 h of milling in bright field and SAED pattern (**a**); comparison of TEM/SAED patterns with XRD diffraction pattern (**b**); TEM micrograph and the elemental distribution of particles by TEM-EDS mapping (**c**).

Sample	BET, m²/g	BJH, m²/g	BJH, cm³/g	BET pore, nm
Mo0 -35 h	1.15	1.05	0.007	19.7
Mo0.1–35 h	1.52	1.27	0.008	16.7
Mo0.25–35 h	0.94	0.81	0.004	17.0
Mo0.25–80 h	9.26	8.14	0.004	15.6
Mo1.0–35 h	1.97	1.65	0.011	18.2

Table 6. Results of the specific surface area measurements.
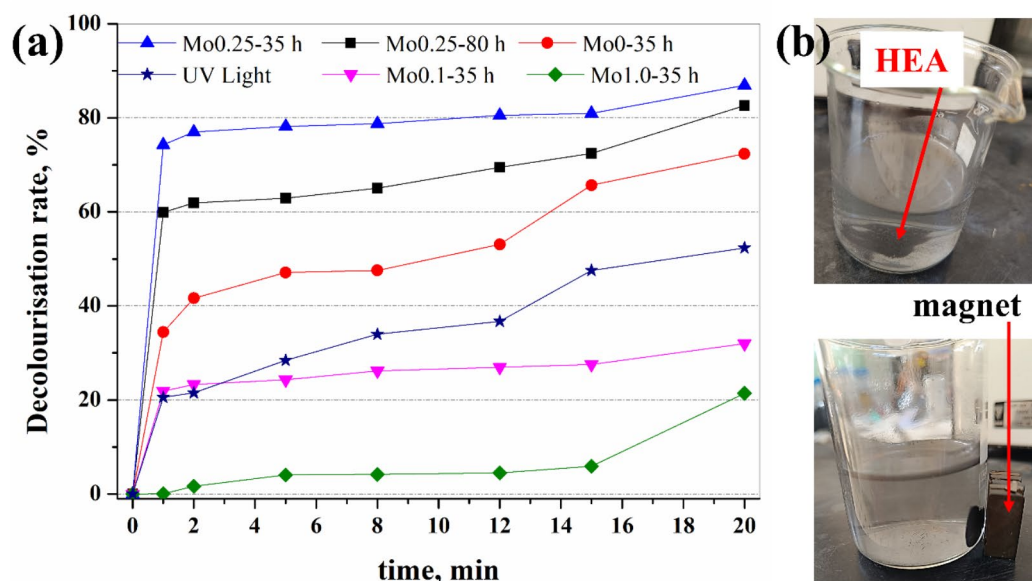
Fig. 7. Influence of milling time and composition on the decolourisation process in the presence of HEAs powder and without HEA powder (**a**). The photo demonstrates the magnetic separability of the HEA particles (**b**).

The specific surface area of HEA powders

The specific surface area is a fundamental property for the catalytic property. The specific surface area was determined using the Brauner–Emmett–Teller (BET) method. After 35 h of milling, the specific surface area of the powders can be considered the same; after 80 h of milling, this value is, of course, increased because the average grain size is reduced (see Table 6). The BET values confirm what was observed in the SEM images, that the surface of the particles is smooth.

Decolourisation analysis

HEAs have attracted increasing attention due to their excellent mechanical and chemical properties[18,37]. Superior catalytic materials are essential to industrial production, reducing emissions, improving equipment productivity, and preventing environmental pollution. The purification of industrial and domestic wastewater hospital effluents has become very important nowadays, as clean drinking water is a great treasure worldwide. Catalytic materials play a significant role in water purification. In the experiment of RhB decolourisation by photo-Fenton catalyst, the nature of the elements that contain the HEA alloy and the size, especially the specific surface area of the alloy powder, play a critical role. High Fenton active elements include Fe. Co promotes the

Fenton effect in a neutral/near-neutral environment[46]. Ti element can improve the catalytic stability of the alloys as well as Ni element. It is well known that TiO_2 oxide has very favourable photocatalytic properties[47]. B. Shen et al.[48] found that Mo^{4+} active sites on the surface of MoO_2 powders can promote RhB decolourisation as it accelerates the rate-limiting step of the process.

Figure 7 shows the decolourisation of Rhodamine B (RhB) as a function of time. The experiments were carried out with the HEA samples and without HEA powders (dark blue star), which was the reference. The results show that the presence of HEA powders accelerated the Fenton oxidation reaction in three cases: Mo0-35 h, Mo0.25–35 h and Mo0.25–80 h. The Mo0.25 sample had the best decolourisation effect over the whole test range after grinding for 35 h and 80 h (Fig. 7). Based on the results, a significant part of the dye decolourisation occurred in the first minutes. The slope of the curves varies significantly over time and can be divided into three phases (periods). The first stage is the first 1 min, the second stage is between 1 and 12 or 15 min, and the third stage is between 12 and 15- and 20 min. After one minute, the M0.25–35 h and 80 h samples had already decolourised 74% and 60% of the initial RhB concentration, respectively. Such an RhB decolourisation effect within one minute has not been found in the literature at room temperature (see Table 7). Between 1 and 12 min, the decolourisation rate does not change quickly over time. At the end of the third stage, after 20 min, maximum decolourisation of Mo 0.25–35 h and 80 h was 87% and 83%, respectively. The Mo0-35 h sample, milled for 35 h without Mo content, decolourised 72% of the RhB after 20 min. The measurement results show that the partial substitution of Co with Mo had a positive catalytic effect on the decolourisation. Comparing the impact of Mo0.25-35 and 80 h of milling, it is surprising at first sight that we would have expected the opposite because, after 80 h of milling, the specific surface area is the largest. Among the phases present on the surface of the powders, the HEA phases with BCC and FCC structures have the better catalytic effect because, in HEA alloys where there are five or more metal elements in one phase, it provides more structural and chemical degrees of freedom to enhance catalytic performance[19,49]. After 80 h of milling, as mentioned above, the number of phases did not change, but the combined amount of BCC and FCC phases decreased by 5 wt%, while the amount of intermetallic phases increased (Table 5).

Surprisingly, a more minor effect than UV light was obtained for Mo0.1–35 h and Mo1.0–35 h (Fig. 7a). One reason for this may be that when looking at the grain size distribution, it can be seen that the Mo1.0–35 h and Mo0.1–35 h samples have the smallest grain size after Mo0.25–80 h and they do not form agglomerates compared to the Mo0.25–80 h sample. Despite continuous mixing, they were not uniformly distributed in the RhB solution. Thus, the floating particles on the surface may have limited the penetration of UV light into the solution. These results suggest that grain size and Mo content have a comparable effect on promoting the Fenton oxidation reaction. The catalysts were tested at 20 °C. These HEA powders have ferromagnetic properties owing to Fe and Ni elements and can easily be separated from the reaction medium without loss by a magnetic field (see Fig. 7b). This is highly favourable for industrial applications, as the $AlCo_{1-x}FeNiTiMo_x$ (x = 0, 0.25).

Conclusion

The formation of different phases in HEA alloys during high-energy milling was investigated. In addition to the AlCoFeNiTi base alloy, the effect of partial substitution of Co by Mo was monitored during a maximum

Catalyst	Reaction condition	Decolourisation rate, %	Time, min	References
Fe_2O_3-Kaolin	Dye: 15 mg/l Catalyst: 1 g/l H_2O_2: 0.05 mol/l pH: 2.21	98	120	[50]
C3–N4@Ag3PW12-30%	Dye: 20 mg/l Catalyst: 0.8 g/l H_2O_2: 0.05 mol/l pH: 2.21	99.4	60	[51]
α-Fe2O3/Fe3O4/g-C3N4 nanocomposites with 5 wt% iron oxide	Dye: 5 ppm catalyst: 018 g	58	180	[52]
$ZnO/ZnMoO_4$	Dye: 20 mg/l Catalyst: 0.4 g/l	83.7	120	[53]
$Fe_{41}Co_7Cr_{15}Mo_{14}C_{15}B_6Y_2$	Dye = 20 mg/l Catalyst = 1 g/l H_2O_2 = 0.002 mM pH = 5 T = 313 K	100	6	[54]
FeCoNiMnCuTi	Dye = 20 mg/l Catalyst = 0.97 g/l H_2O_2 = 1 mM pH = 6 T = 298 K	88	4	[46]
$AlCo_{0.75}FeNiTiMo_{0.25}$	Dye = 5 mg/l Catalyst = 2 g/l H_2O_2 = 21 mM pH = 7.2 T = 298 K	87	20	This work

Table 7. Comparison of RhB decolourisation rate results obtained in this work with the values from the literature.

grinding time of 80 h. Based on empirical rules, a BCC solid solution and an intermetallic phase can be predicted due to the partial replacement of Co by Mo. Two BCC phases, an FCC phase and two $L2_1$ intermetallic phases were formed after 35 h of milling, owing to Mo content. The median values of the pore size distribution were between 2.1 and 0.25 μm. In addition to the AlCoFeNiTi base alloy, a sample containing 5 at% Mo milled for 35 h and 80 h showed excellent catalytic properties in decolourising Rhodamine B using a modified photo-Fenton process. The decolourisation efficiency within 20 min was 72% for the AlCoFeNiTi alloy and 87% for the $AlCo_{0.75}FeNiTiMo_{0.25}$ alloy.

Data availability

The data are available upon request from the corresponding author.

References

1. Yeh, J. W. et al. Nanostructured High-Entropy alloys with multiple principal elements: Novel Alloy Design concepts and outcomes. *Adv. Eng. Mater.* **6**, 299–303 (2004).
2. Cantor, B., Chang, I. T. H., Knight, P. & Vincent, A. J. B. Microstructural development in equiatomic multicomponent alloys. *Mater. Sci. Eng. A* **375–377**, 213–218 (2004).
3. Zhou, Z. C. et al. Effects of aging treatment on microstructure and mechanical properties of non-equiatomic high entropy alloy. *Intermetallics* **153**, 107799 (2023).
4. Li, W. et al. Mechanical property and cellular structure of an additive manufactured FeCoNiCrMo0.2 high-entropy alloy at high-velocity deformation. *J. Mater. Sci. Technol.* **139**, 156–166 (2023).
5. Kang, D. H. & Jung, I. H. Critical thermodynamic evaluation and optimization of the Ag-Zr, Cu-Zr and Ag-Cu-Zr systems and its applications to amorphous Cu-Zr-Ag alloys. *Intermetallics* **18**, 815–833 (2010).
6. Joseph, J. et al. On the enhanced wear resistance of CoCrFeMnNi high entropy alloy at intermediate temperature. *Scr. Mater.* **186**, 230–235 (2020).
7. Yu, Y. et al. A novel Cu-doped high entropy alloy with excellent comprehensive performances for marine application. *J. Mater. Sci. Technol.* **69**, 48–59 (2021).
8. Wang, J. et al. Corrosion-erosion behavior and mechanism of Cu Mo co-doped CoCrFeNi high-entropy alloy coating prepared by directed energy deposition. *Surf. Coat. Technol.* **451**, 129055 (2022).
9. Abdelghany, A. W. et al. Hot deformation behavior and constitutive modeling of a cost-effective Al8Cr12Mn25Ni20Fe35 high-entropy alloy. *J. Alloys Compd.* **928**, 167028 (2022).
10. Varalakshmi, S., Kamaraj, M. & Murty, B. S. Formation and stability of equiatomic and nonequiatomic nanocrystalline CuNiCoZnAlTi high-entropy alloys by mechanical alloying. *Metall. Mater. Trans. A* **41**, 2703–2709 (2010).
11. Liu, S., Gao, M. C., Liaw, P. K. & Zhang, Y. Microstructures and mechanical properties of Al CrFeNiTi0.25 alloys. *J. Alloys Compd.* **619**, 610–615 (2015).
12. Wagner, C. & Laplanche, G. Effects of stacking fault energy and temperature on grain boundary strengthening, intrinsic lattice strength and deformation mechanisms in CrMnFeCoNi high-entropy alloys with different Cr/Ni ratios. *Acta Mater.* **244**, 118541 (2023).
13. Kanyane, L. R., Malatji, N., Popoola, A. P. I. & Fayomi, O. S. I. synthesis of equi-atomic Ti-Al-Mo-Si-Ni high entropy alloy via spark plasma sintering technique: evolution of microstructure, wear, corrosion and oxidation behaviour. *Results Phys.* **14**, 102465 (2019).
14. Shi, P. et al. A precipitate-free AlCoFeNi eutectic high-entropy alloy with strong strain hardening. *J. Mater. Sci. Technol.* **89**, 88–96 (2021).
15. Hu, C., Zhang, J., Zhang, Y., Song, C. & Zhai, Q. A great enhancement of both strength and plasticity in a dual-phase high-entropy alloy by multi-effects of high carbon addition. *Mater. Des.* **225**, 111571 (2023).
16. Vaidya, M., Armugam, S., Kashyap, S. & Murty, B. S. Amorphization in equiatomic high entropy alloys. *J. Non-cryst. Solids* **413**, 8–14 (2015).
17. Fan, C. et al. Rapid amorphization of CrMnFeCoNi high-entropy alloy under ultrasonic vibrations. *Mater. Des.* **225**, 111575 (2023).
18. Zhang, Y. *High-Entropy Materials* (Springer Singapore, 2019). https://doi.org/10.1007/978-981-13-8526-1
19. Wang, B. et al. Understanding the enhanced catalytic activity of high entropy alloys: from theory to experiment. *J. Mater. Chem. A* **9**, 19410–19438 (2021).
20. Kumar Katiyar, N., Biswas, K., Yeh, J. W. & Sharma, S. Sekhar Tiwary, C. A perspective on the catalysis using the high entropy alloys. *Nano Energy* **88**, 106261 (2021).
21. Yu, L. et al. High-entropy alloy catalysts: from bulk to nano toward highly efficient carbon and nitrogen catalysis. *Carbon Energy* **4**, 731–761 (2022).
22. Xie, P. et al. Highly efficient decomposition of ammonia using high-entropy alloy catalysts. *Nat. Commun.* **10**, 4011 (2019).
23. Du, P. & Eisenberg, R. Catalysts made of earth-abundant elements (Co, Ni, Fe) for water splitting: Recent progress and future challenges. *Energy Environ. Sci.* **5**, 6012 (2012).
24. Mei, Y. et al. High-entropy alloy with Mo-coordination as efficient electrocatalyst for oxygen evolution reaction. *ACS Catal.* **12**, 10808–10817 (2022).
25. Zhao, J. et al. Fast joule heating synthesis of NiCoFeCrMo high-entropy alloy embedded in graphene for water oxidation. *J. Alloys Compd.* **966**, 171535 (2023).
26. Li, P. et al. A single-phase feconimnmo high-entropy alloy oxygen evolution anode working in alkaline solution for over 1000 h. *ACS Catal.* **12**, 11667–11674 (2022).
27. Fu, Y., Li, J., Luo, H., Du, C. & Li, X. Recent advances on environmental corrosion behavior and mechanism of high-entropy alloys. *J. Mater. Sci. Technol.* **80**, 217–233 (2021).
28. Anand Sekhar, R., Bakshi, S. R. & Microstructural Cr,Co,Fe)-Based high-entropy alloys processed through mechanical alloying. *Trans. Indian Inst. Met.* **72**, 1427–1430 (2019).
29. Anand Sekhar, R., Samal, S., Nayan, N. & Bakshi, S. R. Microstructure and mechanical properties of Ti-Al-Ni-Co-Fe based high entropy alloys prepared by powder metallurgy route. *J. Alloys Compd.* **787**, 123–132 (2019).
30. Avila-Rubio, M. A. et al. Effect of Mo and Ti on the microstructure and microhardness in AlCoFeNiMoTi high entropy alloys prepared by mechanical alloying and conventional sintering. *Adv. Powder Technol.* **31**, 1693–1701 (2020).
31. Mishra, R. K., Shahi, R. R., Singh, A. R. & Sahay, P. P. Synthesis, characterizations, and magnetic properties of FeCoNiTi-based high-entropy alloys. *Emergent Mater.* **3**, 655–662 (2020).
32. Łoński, W. et al. Microstructure, magnetic properties, corrosion resistance and catalytic activity of dual-phase AlCoNiFeTi and AlCoNiFeTiSi high entropy alloys. *J. Alloys Compd.* **934**, 167827 (2023).

33. Baldenebro-Lopez, F. J., Herrera-Ramírez, J. M., Arredondo-Rea, S. P., Gómez-Esparza, C. D. & Martínez-Sánchez, R. Simultaneous effect of mechanical alloying and arc-melting processes in the microstructure and hardness of an AlCoFeMoNiTi high-entropy alloy. *J. Alloys Compd.* **643**, S250–S255 (2015).

34. GUO, S. & LIU, C. T. Phase stability in high entropy alloys: formation of solid-solution phase or amorphous phase. *Progress Nat. Science: Mater. Int.* **21**, 433–446 (2011).

35. Zhang, Y., Zhou, Y. J., Lin, J. P., Chen, G. L. & Liaw, P. K. Solid-solution phase formation rules for multi-component alloys. *Adv. Eng. Mater.* **10**, 534–538 (2008).

36. Yang, X. & Zhang, Y. Prediction of high-entropy stabilized solid-solution in multi-component alloys. *Mater. Chem. Phys.* **132**, 233–238 (2012).

37. Gao, M. C., Yeh, J. W. & Peter, K. & Zhang, Y. High-Entropy Alloys: Fundamentals and Applications (Springer International Publishing, 2016).

38. Takeuchi, A. & Inoue, A. Calculations of mixing enthalpy and mismatch entropy for ternary amorphous alloys. *Mater. Trans. JIM* **41**, 1372–1378 (2000).

39. Alam, I., Adaan-Nyiak, M. A. & Tiamiyu, A. A. Revisiting the phase stability rules in the design of high-entropy alloys: a case study of quaternary alloys produced by mechanical alloying. *Intermetallics* **159**, 107919 (2023).

40. Chen, Y. L., Hu, Y. H., Hsieh, C. A., Yeh, J. W. & Chen, S. K. Competition between elements during mechanical alloying in an octonary multi-principal-element alloy system. *J. Alloys Compd.* **481**, 768–775 (2009).

41. He, J. Y. et al. Effects of Al addition on structural evolution and tensile properties of the FeCoNiCrMn high-entropy alloy system. *Acta Mater.* **62**, 105–113 (2014).

42. Sort, J., Nogués, J., Suriñach, S. & Baró, M. D. Microstructural aspects of the hcp-fcc allotropic phase transformation induced in cobalt by ball milling. *Phil. Mag.* **83**, 439–455 (2003).

43. Liu, S., Cao, P., Lin, D. Y. & Tian, F. Stability of L21 (NiM)2TiAl (M = Co, Fe) in high-entropy alloys. *J. Alloys Compd.* **764**, 650–655 (2018).

44. Vallimanalan, A. et al. Corrosion behaviour of thermally sprayed Mo added AlCoCrNi high entropy alloy coating. *Mater. Today: Proc.* **27**, 2398–2400 (2020).

45. Schuster, J. C. & Palm, M. Reassessment of the binary Aluminum-Titanium phase diagram. *JPED* **27**, 255–277 (2006).

46. Wang, N. FeCoNiMnCuTi high entropy amorphous alloys and M50Ti50 (M = fe, Cu, FeCoNiMnCu) amorphous alloys: Novel and efficient catalysts for heterogeneous photo-Fenton decomposition of rhodamine B. *Surf. Interfaces* **33**, 102265 (2022).

47. Eldoma, M. A. et al. Enhancing photocatalytic performance of Co-TiO2 and Mo-TiO2-based catalysts through defect engineering and doping: a study on the degradation of organic pollutants under UV light. *J. Photochem. Photobiol. A* **446**, 115164 (2024).

48. Shen, B. et al. (III)/Fe(II) cycling triggered by MoO2 in Fenton reaction for the degradation of dye molecules and the reduction of cr(VI). *Chin. Chem. Lett.* **30**, 2205–2210 (2019).

49. Qiu, H. J. et al. Noble Metal-Free Nanoporous High-Entropy alloys as highly efficient electrocatalysts for Oxygen Evolution reaction. *ACS Mater. Lett.* **1**, 526–533 (2019).

50. Guo, S., Zhang, G. & Wang, J. Photo-Fenton degradation of rhodamine B using Fe 2 O 3 –Kaolin as heterogeneous catalyst: characterization, process optimization and mechanism. *J. Colloid Interface Sci.* **433**, 1–8 (2014).

51. Khan, A. et al. Novel and facile strategy for immobilization of Ag3PW12 crystals on graphitic carbon nitride (g-C3-N4) sheets, a superior photocatalyst for decomposition of organic waste. *J. Solid State Chem.* **329**, 124405 (2024).

52. Afkari, M., Masoudpanah, S. M., Hasheminiasari, M. & Alamolhoda, S. Effects of iron oxide contents on photocatalytic performance of nanocomposites based on g-C3N4. *Sci. Rep.* **13**, 6203 (2023).

53. Firmansyah, R., Bakri, R. & Yulizar, Y. Enhancement of photocatalytic activity of ZnO by ZnMoO4 compositing under visible light via hydrothermal green synthesis. *Inorg. Chem. Commun.* **155**, 110893 (2023).

54. Tao, X., Chen, Q., Ji, L. & Huang, G. The synergy of chromium and molybdenum on the stable catalysis of Fe-based amorphous alloy powder. *J. Non-cryst. Solids* **570**, 121010 (2021).

Acknowledgements

Author contributions

M. Sveda: Investigation, data curation, F. Kristály: methodology, formal analysis, E. Sikora: methodology, formal analysis, A. Sycheva: methodology, G. Karacs: methodology, T. Ferenczi: methodology, D. Janovszky: Conceptualization, editing, writing- original draft, review and editing. All authors have read and agreed to the published version of the manuscript.

Competing interests

The authors declare no competing interests.

Additional information

Correspondence and requests for materials should be addressed to D.J.

Reprints and permissions information is available at www.nature.com/reprints.

Publisher's note Springer Nature remains neutral with regard to jurisdictional claims in published maps and institutional affiliations.